



HAL
open science

Interleaved Parasitic Arrays Antenna (IPAA) for Active VSWR Mitigation in Large Phased Array Antennas With Wide-Angle Scanning Capacities

Remy Lamey, Marc Thevenot, Cyrille Menudier, Eric Arnaud, Olivier Maas, Faycel Fezai

► **To cite this version:**

Remy Lamey, Marc Thevenot, Cyrille Menudier, Eric Arnaud, Olivier Maas, et al.. Interleaved Parasitic Arrays Antenna (IPAA) for Active VSWR Mitigation in Large Phased Array Antennas With Wide-Angle Scanning Capacities. IEEE Access, 2021, 9, pp.121015 - 121030. 10.1109/access.2021.3108231 . hal-03410147

HAL Id: hal-03410147

<https://hal.science/hal-03410147>

Submitted on 31 Oct 2021

HAL is a multi-disciplinary open access archive for the deposit and dissemination of scientific research documents, whether they are published or not. The documents may come from teaching and research institutions in France or abroad, or from public or private research centers.

L'archive ouverte pluridisciplinaire **HAL**, est destinée au dépôt et à la diffusion de documents scientifiques de niveau recherche, publiés ou non, émanant des établissements d'enseignement et de recherche français ou étrangers, des laboratoires publics ou privés.

Received August 4, 2021, accepted August 19, 2021, date of publication August 26, 2021, date of current version September 8, 2021.

Digital Object Identifier 10.1109/ACCESS.2021.3108231

Interleaved Parasitic Arrays Antenna (IPAA) for Active VSWR Mitigation in Large Phased Array Antennas With Wide-Angle Scanning Capacities

RÉMY LAMEY^{1,2}, MARC THEVENOT², CYRILLE MENUDIER², (Member, IEEE),
ERIC ARNAUD², OLIVIER MAAS¹, AND FAYCEL FEZAI¹, (Member, IEEE)

¹Thales Land & Air Systems, 91470 Limours, France

²XLIM UMR CNRS 7252, University of Limoges, 87000 Limoges, France

Corresponding author: Marc Thevenot (marc.thevenot@xlim.fr)

This work was supported in part by the French State handled by the National Research Agency for the “Programme Investissements d’Avenir” under the reference ANR-17-SATE-0004 with the “Agence Aliénor Transfert” in the Region “Nouvelle-Aquitaine,” under the contract SYNTOSA–Synthesis of active VSWR for antennas.

ABSTRACT This paper explores a new concept for the design of high scanning-range phased array antennas: the Interleaved Parasitic Arrays Antenna or IPAA. In this concept, we use periodic parasitic elements and the generator impedance to control the Active Voltage Standing Wave Ratio (AVSWR) over a wide scanning range. This new array architecture comes with a design methodology enabling a smooth step-by-step design process aiming at reducing the need for full-wave calculations. First, a numerical dual-polarization design is presented in detail to illustrate the methodology and to give the design keys to the reader. Then, a prototype working in the 5G C-band between 3.4 and 3.8 GHz (11% bandwidth) was designed using this methodology and measured for a 36-element array. It is meant to demonstrate and validate the mutual coupling management done by the interleaved parasitic arrays and the design process accuracy. Good correspondence between measurements and simulation was found and the proposed unit cell with its corresponding tile can be integrated in a larger phased array with active modules to perform beam steering over an important scanning range without deteriorating the AVSWR. The proposed unit cell is designed for a high-scanning range going from $\theta = 0^\circ$ to $\theta = 70^\circ$ for every φ -directions and shows an active reflection coefficient for an infinite array below -13.6 dB.

INDEX TERMS 5G, active antenna arrays, active voltage standing wave ratio (AVSWR), antenna arrays, beam steering, C-band, impedance matching, mutual couplings, parasitic elements, periodic structures, superstrate.

I. INTRODUCTION

Large planar antenna arrays often suffer from high mutual coupling between their radiating elements that can cause scan blindness. This phenomenon can be seen through the Active Voltage Standing Wave Ratio (AVSWR), which corresponds to the variation of the reflection coefficient while the beam is scanned and all elements are fed, taking into account mutual coupling interactions. This effect corresponds to the variation of the active input impedance at the feeding point of the array. Another common equivalent representation is based on the active reflection coefficient, expressed in dB.

A simple solution would be to try decreasing and eliminating mutual coupling in the array. One can achieve that

The associate editor coordinating the review of this manuscript and approving it for publication was Giorgio Montisci¹.

by increasing the spacing between the driven elements but it can cause grating lobes to occur, thus reducing the scanning performances of the array.

There are some techniques to achieve mutual coupling reduction like Electromagnetic Band Gap (EBG) [1], [2] and Defected Ground Structures (DGS) [3] which have been widely studied in the literature and have shown an increase in performances for the array.

According to Stein [4], mutual coupling is certain in dense antenna arrays because the elements patterns in a dense array will overlap. Hannan [5] and Kahn [6] then confirmed this statement and Kahn stated that the maximum possible efficiency of the array is set by the array organization.

These conclusions show that we cannot eliminate mutual couplings in a dense antenna array. Thus, in case of large periodic arrays, the unit cell has to be studied in terms

of AVSWR because mutual coupling cannot be totally removed.

Another approach is to control the mutual coupling instead of trying to reduce it. Several approaches like the connected array, PUMA, WAIM (Wide-Angle Impedance Matching) structures and corrective coupling techniques have shown great results in mitigating the AVSWR of the array elements.

For example, the synthesis of multilayered WAIM [7] have been done using an iterative method giving a very efficient way to compute and synthesize the multilayered WAIM on an important frequency bandwidth (~18%) and scanning range. Other solutions like PUMA [8] enable ultra-wide band performances with a good scanning range, at the expense of a significant manufacturing complexity. Connected arrays [9] also show very high bandwidth performances and scanning range capabilities in terms of AVSWR, even if the manufacturing process, especially with dipoles can be a limitation to a practical use case. As an alternative solution, the corrective coupling technique [10] enabled an increased scanning range from 48° to 65° by using microstrip lines to compensate for the effects of surface waves. However, the impact of these corrective lines on the radiation patterns cannot be neglected. All these solutions involving the control of mutual couplings are complex but they exhibit good performances.

In this paper, the new concept of Interleaved Parasitic Arrays Antenna (IPAA) is defined. The originality of this work is to define a reliable formalism to study the unit cell of an antenna array which is able to mitigate the AVSWR thanks to additional parasitic elements. The main idea is to define a macro-cell including these elements to improve the scanning performances of the final antenna, using the couplings as degrees of freedom. One of the main advantages is to use conventional microstrip circuit stacking, reducing the complexity without degrading the performances. Another important criterion to justify the IPAA is its ability to keep a regular lattice and a technology suited to RFIC integration for a beam forming network using distributed amplification with phase shifters [11], [12]. Moreover, the formalism presented to solve the problem is based on a combination of small full wave (FW) simulations and analytical formulations to avoid extensive and costly FW simulations or brute force parameterization.

This manuscript explains in detail the architecture of the IPAA before explaining the synthesis algorithm and the design methodology. The synthesis algorithm is used to design a unit cell for double polarization operations in order to illustrate the methodology. Then, the design steps of a high performance 5G unit cell are shown with its predicted performances. Finally, a prototype was built and measured to validate both the methodology and the technology.

II. CONCEPT DEFINITION AND DESIGN METHODOLOGY

A. DEFINITION OF THE IPAA CONCEPT

The objective is to produce designs of radiating panels with wide-angle scanning capacities over a specified frequency

band with low AVSWR. To this aim, it is interesting to remind some historical works to define our objectives. As Hannan mentioned in his 1964 paper [5], it is now widely known that couplings are unavoidable in dense antenna arrays and the active impedances in large arrays are naturally sensitive to the beam steering. In [13], Pozar established the relation between the active reflection coefficient and the active element gain pattern (AEP) (which is the radiation pattern of an active element while all other inactive elements in the array are connected to the impedances of the inactive generators): the shape of the AEP is linked to the angular dependency of the AVSWR. It also means that an AEP without nulls or deep in the scanning range is a sufficient condition to guarantee the beam steering performances of a full array without suffering from scan blindness. Moreover, considering the fact that the impedance of the inactive generators surrounding an excited element directly affects its element pattern [5], the generator impedance (which is the same for all elements) appears as an obvious way to optimize the AVSWR over the scanning range.

In our work, we first use this fundamental property as a starting point for a global optimization considering both the AVSWR and the AEP. Furthermore, we propose to introduce parasitic elements [14] in each cell of the periodic array, without increasing the spacing between the cells. These parasitic elements are connected to reactive loads, which allow controlling the electromagnetic field distribution inside and between each cell.

The goal of our global optimization is to find the best working point of a two-way optimization (the set: reactive loads – generator impedance), i.e. the combination which will provide both active matching and an active element gain pattern exhibiting a ‘cosθ’ dependent gain pattern. This corresponds to the ideal AEP characteristics [15], [16]. Hence, this global optimization aims at minimizing the AVSWR on a set of radiation directions considering the generator impedance for the matching.

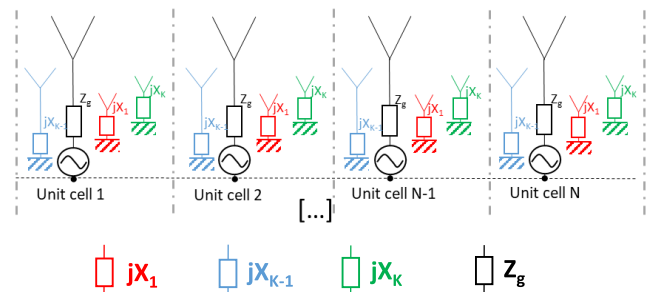


FIGURE 1. Interleaved Parasitic Antenna Array principle—Main array in black and parasitic ones in red, green and blue.

Figure 1 introduces the array architecture composed of periodic cells, each containing at least one driven element connected to its generator impedance Z_g and a set of parasitic elements paired with their reactive load.

This architecture is an interleaving of K parasitic arrays with a driven one. The passive reactive loads X_1 to X_k and the generator impedance Z_g of the driven elements set the interactions between these arrays. By physically changing the combination of couplings and therefore the reflected waves inside the feeding ports of the driven antenna array, these K parasitic arrays aim at mitigating the active VSWR through an appropriately defined optimization process. In other words, the parasitic elements can be used to obtain a wide angle impedance scanning.

The reactive loads and the generator impedance can be determined by the synthesis process described in the next part, provided a set of specifications in terms of gain and AVSWR.

B. FORMALIZATION OF THE SYNTHESIS ALGORITHM

Our development aims at solving this electromagnetic problem without requiring expensive full-wave parametric simulations. The optimization is global, meaning the AVSWR has to be minimized over a set of radiated directions and for a specified frequency band. As explained in part A, this global optimization consists in finding the optimum generator impedances and associated reactive loads. The solutions are searched for infinite arrays making this optimization suitable and accurate for large arrays.

The first stage is based on the use of a full-wave simulator (e.g. CST Studio Suite) to compute the interactions between the interleaved arrays using Floquet’s formalism [17]. Such a simulator is now common and widely used by antenna designers. The scheme of a simulated unit cell is given in Fig. 2. The computational volume contains the driven element(s) and the K parasitic antennas. The sidewalls of the computational volume are bounded by periodic conditions that emulate the infinite periodicity of the interleaved arrays. A Floquet’s port closes the volume along the third dimension. Moreover, the periodic boundaries set the phase slope between cells according to the beam direction $\{\theta_i; \varphi_i\}$.

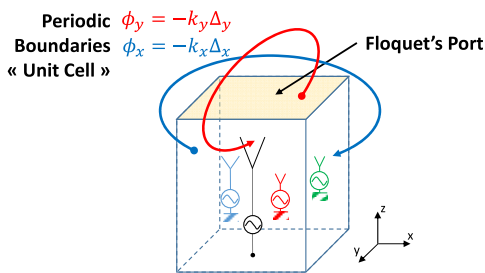


FIGURE 2. Boundary conditions of the computational volume for the IPAA unit cell.

Simulations are done for sampled scan angles $\{\theta_i; \varphi_i\}$, providing the active scattering matrices S_{active} for these radiation directions. These simulations are inexpensive but they accurately mesh the cell since the computational volume is relatively small. We name “active scattering matrix”, the matrix containing the interactions between the $k + 1$ antennas in this

periodic cell (Fig. 2). These matrices are obtained for generators having the 50Ω standard normalization impedance.

For the sake of clarity and versatility in most practical applications, we now describe the general case of having two active probes in each cell in order to be compliant with the radiation of dual-orthogonal polarizations. Figure 3 shows an active-matrix schematic for a dual-polarized cell with k parasitic antennas. This schematic is dependent on the steering direction $\{\theta_i, \varphi_i\}$. Moreover, the matrix that is extracted from each simulation (i.e. each scan angle) contains information about the coupling of the two radiating modes in the Floquet’s ports. This enables to calculate the XPD (Cross Polarization Discrimination) during the optimization.

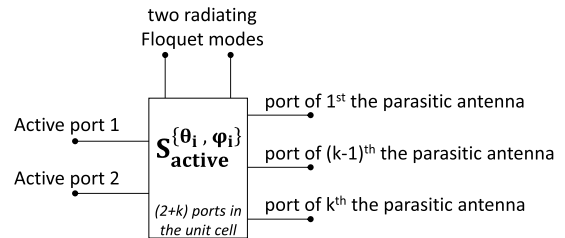


FIGURE 3. Elements of the active scattering matrix for a dual-polarization unit cell.

Once the active scattering matrices are known for a representative sample of steering directions within the desired scanning range, they become the unique material useful for the optimization.

Therefore, the algorithm must determine the passive reactive loads to pair up with the K parasitic antennas, and the impedances of both generators connected to the active ports of the cell. This optimization enables reaching the objectives such as the impedance matching of active ports or the quality of the radiated polarizations. This search is an iterative process, which can be driven by optimization toolboxes available in many commercial softwares.

Before dealing with the iterative optimization, the dimensions of the problem must be reduced. This is possible when reactive loads are connected to the parasitic elements ports (see Fig. 4).

The active scattering matrices are normalized by the standard impedance $Z_0 = 50\Omega$. Each reactive load X_1 to X_k becomes a reflection coefficient for the outgoing normalized waves traveling from the multipole through the ports number 3 to number $k + 2$. The reflection coefficient is written in equation (1).

$$\Gamma_n(\omega) = \frac{j \cdot X_{n-2}(\omega) - 50}{j \cdot X_{n-2}(\omega) + 50} \quad (n \in \{3, \dots, k + 2\}) \quad (1)$$

According to notations a_n and b_n for the normalized waves traveling through the $k + 2$ ports of the active scattering matrix (Fig. 5), we can operate the reduction of the system

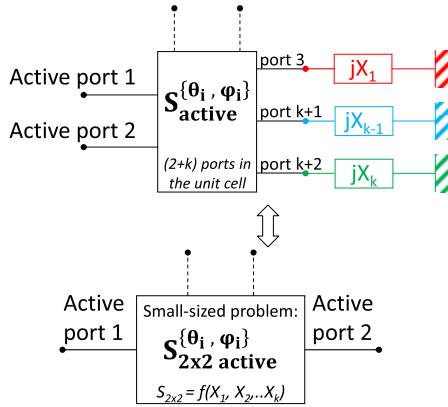


FIGURE 4. a) Active scattering matrix connected with the reactive loads. b) Reduced active scattering matrix.

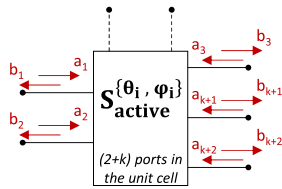


FIGURE 5. Multipole representation of the active scattering matrix with normalized inward and outward traveling waves.

with the reflection coefficients Γ_n on parasitic antennas:

$$\begin{pmatrix} a_1 \\ a_2 \\ a_3 \\ \vdots \\ a_{k+2} \end{pmatrix} = \begin{pmatrix} a_1 \\ a_2 \\ \Gamma_3 \cdot b_3 \\ \vdots \\ \Gamma_{k+2} \cdot b_{k+2} \end{pmatrix}$$

Moreover, from figure (5), we have (Equation 2)

$$\vec{b} = [S_{active}^{\theta_i, \varphi_i}] \cdot \vec{a} \quad (2)$$

With $[\Gamma] = \text{diag} \begin{pmatrix} 0 \\ 0 \\ \Gamma_3 \\ \vdots \\ \Gamma_{k+2} \end{pmatrix}$ and $\vec{a} = \begin{pmatrix} a_1 \\ a_2 \\ a_3 \\ \vdots \\ a_{k+2} \end{pmatrix}$, all the

waves in the multipole are defined by those in the active ports, numbered 1 and 2 (equations 3, 4).

$$\vec{a} = [\Gamma] \cdot [S_{active}^{\theta_i, \varphi_i}] \cdot \vec{a} + \begin{pmatrix} a_1 \\ a_2 \\ 0 \\ \vdots \\ 0 \end{pmatrix} \quad (3)$$

$$(3) \xrightarrow{\text{yields}} \vec{a} = ([I] - [\Gamma] \cdot [S_{active}^{\theta_i, \varphi_i}])^{-1} \cdot \begin{pmatrix} a_1 \\ a_2 \\ 0 \\ \vdots \\ 0 \end{pmatrix} \quad (4)$$

Using the notation $M = ([I] - [\Gamma] \cdot [S_{active}^{\theta_i, \varphi_i}])^{-1}$, (5) gives the reduced active scattering matrix of the system in fig. 4-b. Each of the four inner terms is a result of a matrix product:

$$S_{2 \times 2}^{\theta_i, \varphi_i} = \begin{bmatrix} S_{active}^{\theta_i, \varphi_i}(1, :) * M(:, 1) & S_{active}^{\theta_i, \varphi_i}(1, :) * M(:, 2) \\ S_{active}^{\theta_i, \varphi_i}(2, :) * M(:, 1) & S_{active}^{\theta_i, \varphi_i}(2, :) * M(:, 2) \end{bmatrix} \quad (5)$$

The optimization defined in part A adjusts the generator impedances Z_{g1} and Z_{g2} in order to act on the active element pattern. This means that the reduced matrix (5), which is normalized to the 50Ω impedance, must be connected to these adjustable impedances.

Only for a dual polarization case, the optimization process needs the knowledge of the generator impedances to be performed. This is due to the internal couplings between both driven ports.

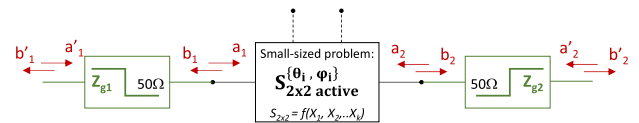


FIGURE 6. Reduced active scattering matrix connected to the generator impedances Z_{g1} and Z_{g2} .

We introduce the impedance step in the optimization chain:

$$S_{step}^{(Z_{g1} \text{ to } 50\Omega)} = \begin{bmatrix} \frac{50 - Z_{g1}^*}{50 + Z_{g1}} & \frac{2 * \sqrt{\text{Real}(Z_{g1}) * 50}}{50 + Z_{g1}} \\ \frac{2 * \sqrt{\text{Real}(Z_{g1}) * 50}}{50 + Z_{g1}} & \frac{Z_{g1} - 50}{50 + Z_{g1}} \end{bmatrix} \quad (6)$$

$$S_{step}^{(50\Omega \text{ to } Z_{g2})} = \begin{bmatrix} \frac{Z_{g2} - 50}{50 + Z_{g2}} & \frac{2 * \sqrt{\text{Real}(Z_{g2}) * 50}}{50 + Z_{g2}} \\ \frac{2 * \sqrt{\text{Real}(Z_{g2}) * 50}}{50 + Z_{g2}} & \frac{50 - Z_{g2}^*}{50 + Z_{g2}} \end{bmatrix} \quad (7)$$

In the optimization loop, the three matrices (6), (5) and (7) are cascaded. On the one hand, the interactions with the parasitic antennas are set in (5), adjusting the phases of the reflection coefficients Γ_3 to Γ_{k+2} . On the other hand, the impedances of the active generators Z_{g1} and Z_{g2} vary through both matrices (6) and (7).

The system in Fig. 6 is a global 2×2 matrix in which the four coefficients depends on the generator impedances and the reactive loads paired with the parasitic elements.

Chaining (6), (5) and (7) (see Fig. 6) leads to the global matrix (8):

$$S_{GLOBAL}^{\theta_i, \varphi_i} \Big|_{Z_{g1}, Z_{g2}, \Gamma_3, \dots, \Gamma_{k+2}} = \begin{bmatrix} S_{11GLOBAL}^{active}(\omega, \theta_i, \varphi_i) & S_{12GLOBAL}^{active}(\omega, \theta_i, \varphi_i) \\ S_{21GLOBAL}^{active}(\omega, \theta_i, \varphi_i) & S_{22GLOBAL}^{active}(\omega, \theta_i, \varphi_i) \end{bmatrix} \quad (8)$$

We formulate as many “GLOBAL” matrices as the number of steering directions samples. The optimization loop adjusts both generator impedances and the reactive loads to minimize the 4 terms of the matrix simultaneously for all steering angles and over the frequency band.

The knowledge of the traveling waves at any connections between the blocks (Fig. 6) enables computing the weights for both radiated Floquet’s modes. Therefore, the methodology allows calculating the antenna efficiency and the cross polarization discrimination for each steering angle. Maximizing the XPD can be an additional target for the optimization.

Notice that before any optimization it is efficient to choose a driven element granting minor frequency dispersion over the desired bandwidth.

Part C illustrates the formalism using a Matlab optimization toolbox for practical implementation. The choice for the optimization algorithm is outside the scope of this article, but notice that many other solutions can be relevant to solve the presented set of equations.

C. DESIGN METHODOLOGY IMPLEMENTATION

We propose these numerical examples solving some of the most complex optimization cases. Indeed, these cases represent several global constrained optimizations done for two linear polarizations and it implies minimizing the four components of the reduced GLOBAL matrix (8). The optimizations are realized on several fractional bandwidth around the center frequencies f_n with different criterions on the cross polarization discrimination (XPD) and for a wide scanning range considering the directions $\{\theta_i; \varphi_i\}$ defined as $0^\circ \leq \theta_i \leq 60^\circ$ and $0^\circ \leq \varphi_i \leq 360^\circ$.

CAD models from CST MWS of the considered cells are shown in Fig. 7a & 7b. The different PCB used in the designs are Taconic TLY-5 with a relative permittivity $\epsilon_r = 2.2$. The metals are set as PEC (Perfect Electric Conductors).

The driven element is a cavity backed stacked patches element fed by two coaxial probes connected to the lower patch to enable dual polarization.

Two different functionalized superstrates are tested for the different optimization cases:

- A 2D superstrate composed of one group of 2 parasitic crossed-dipoles (Fig. 7a: Ports 3 & 4);
- A 3D superstrate composed of one group of 2 parasitic crossed-dipoles (Fig. 7b: Ports 6 & 7), a group of 2 parasitic monopoles (Fig. 7b: Ports 3 & 4) located on the middle of the cell edge, a single parasitic monopole (Fig. 7b: Port 5) set in the cell corner and a parasitic control (Fig. 7b: Port 8) under the driven patch.

In a group of parasitic elements, each reactive load is set to be identical in the optimizer. The choice of the parasitic elements, i.e. dipoles or monopoles, is based on their compactness for integration, especially to encircle the unit cell to stimulate the couplings. Their location is also chosen to keep as much as possible the symmetry of the unit cell while the array is fully built. To avoid sharing monopoles on the boundary conditions, the distribution of Fig. 7b on

each side has been chosen, resulting in the regular subarray of monopoles in Fig.9. Notice that these ones are not joining the boundary conditions of the unit cell. Other arrangements can also be imagined by the designer.

These superstrate are respectively illustrated in Fig. 7a and Fig. 7b. The filling of the cavity and the spacer are set to vacuum. All dimensions of the structure are given in table 1 as a function of the element spacing Δ and reported on the unit cell design in Fig. 7c. Notice that Δ is chosen close to a half-wavelength in free space to avoid grating lobes.

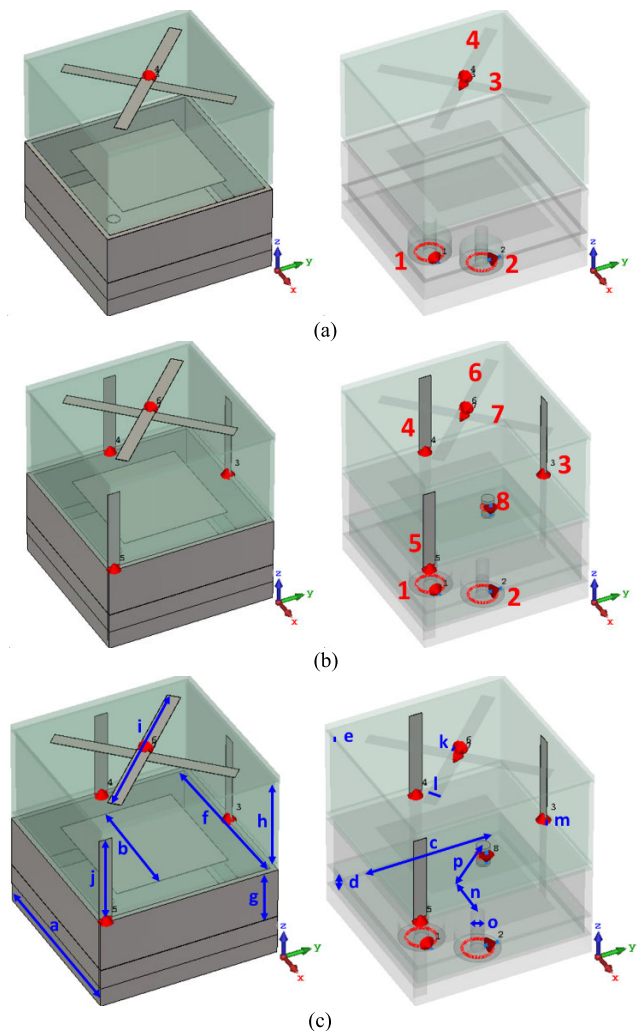


FIGURE 7. a) Unit cell of a dual-polarization IPAA with a 2D superstrate. b) Unit cell of a dual-polarization IPAA with a 3D superstrate with isolation control. c) Unit cell of a dual-polarization IPAA annotated with Table 1 dimensions.

A decoupling control mechanism is connected under the driving patch of the unit cell with the 3D superstrate (Fig. 7b) giving a total of 5 degrees of freedom for the optimization (Generator impedance Z_g , dipoles reactive loads, side monopoles reactive loads, corner monopole reactive load, decoupling control reactive load). In comparison, the cell with the 2D superstrate (Fig. 7a) is optimized with 2 degrees of freedom (Z_g , dipoles reactive loads). The decoupling

TABLE 1. Dimensions of the unit cell components.

Parameter Names	Index letter	Dimensions
Unit cell period	a	Δ
Upper square patch length	b	$0.6282*\Delta$
Lower square patch length	c	$0.7260*\Delta$
Lower PCB thickness	d	$0.114*\Delta$
Superstrate PCB thickness	e	$36.78E-3*\Delta$
Cavity length	f	$0.9422*\Delta$
Cavity height	g	$0.2896*\Delta$
Spacer height	h	$0.5068*\Delta$
Total horizontal dipole length	i	$0.9702*\Delta$
Vertical monopole length	j	$0.4778*\Delta$
Dipole middle gap	k	$14.48E-3*\Delta$
Monopole & Dipole width	l	$72.4E-3*\Delta$
Monopole gap with metallic cavity	m	$14.48E-3*\Delta$
Feeding probe distance from cell center	n	$0.2107*\Delta$
Feeding probe diameter	o	$72.4E-3*\Delta$
Isolation control probe from cell center	p	$0.2889*\Delta$

control mechanism gives a degree of freedom enabling to act on the feeding isolation and on the XPD. The isolation control port is integrated as a parasitic port (port number 8 on fig. 7b) in the optimization process and works the same way as the parasitic elements.

The optimization cases are done for several frequency bands with center frequencies f_n . The frequencies are defined as a function of element spacing Δ . This means that the cell geometry is the same for every optimization cases but the optimization frequency band is different. Three center frequencies are defined for 4 optimizations:

$$f_1 * \frac{\Delta}{c} = 0.437 \tag{9}$$

$$f_2 * \frac{\Delta}{c} = 0.460 \tag{10}$$

$$f_3 * \frac{\Delta}{c} = 0.483 \tag{11}$$

f_n corresponds to the center frequency of the optimization case [s^{-1}]

Δ is the element spacing staying constant for all optimization cases [mm]

c is the speed of light in vacuum [$mm \cdot s^{-1}$]

Looking at Equations (9), (10) and (11), f_3 corresponds to the highest center frequency and is close to half wavelength element spacing meaning that the proximity of grating lobes will affect the AVSWR.

The active scattering coefficients S'_{11} , S'_{21} , S'_{12} and S'_{22} are calculated from the four traveling waves a'_1 , b'_1 , a'_2 and b'_2 seen in Fig. 6. These scattering coefficients are summarized for the two simulated unit cells considering different optimization cases in Table 2 and Figure 8.

Figure 8 represents the active S'_{11} for the three first optimization cases from table 2 considering the 2D superstrate and the 3D superstrate with isolation control. It has been calculated using the schematic detailed in Fig. 6.

TABLE 2. Performances of the unit cell considering different optimization scenarios active (S'_{11} , S'_{21} , S'_{12} , S'_{22}) and XPD are expressed in dB.

Optimization cases	2D superstrate		3D superstrate + isolation control	
	Active (S'_{11} ; S'_{21})	XPD	Active (S'_{11} ; S'_{21})	XPD
$[0.95 - 1.05]f_1$	-13.3 ; -15.5	18.3	-13.8 ; -15.2	19.8
$[0.95 - 1.05]f_2$	-12.6 ; -17.4	17.5	-14.1 ; -14.2	21.1
$[0.95 - 1.05]f_3$	-8.1 ; -12.1	11.1	-13.2 ; -13.1	18.1
$[0.9 - 1.1]f_2$	-5.6 ; -12.6	11.5	-10.5 ; -14.3	17.4

The optimization bandwidths are contained between the vertical red bars for each graph. This figure illustrates how the parasitic elements affect the active S'_{11} differently according to the different optimization cases.

OPTIMIZED UNIT CELL ACTIVE S'_{11} FOR THE 3 FIRST CASES OF TABLE II

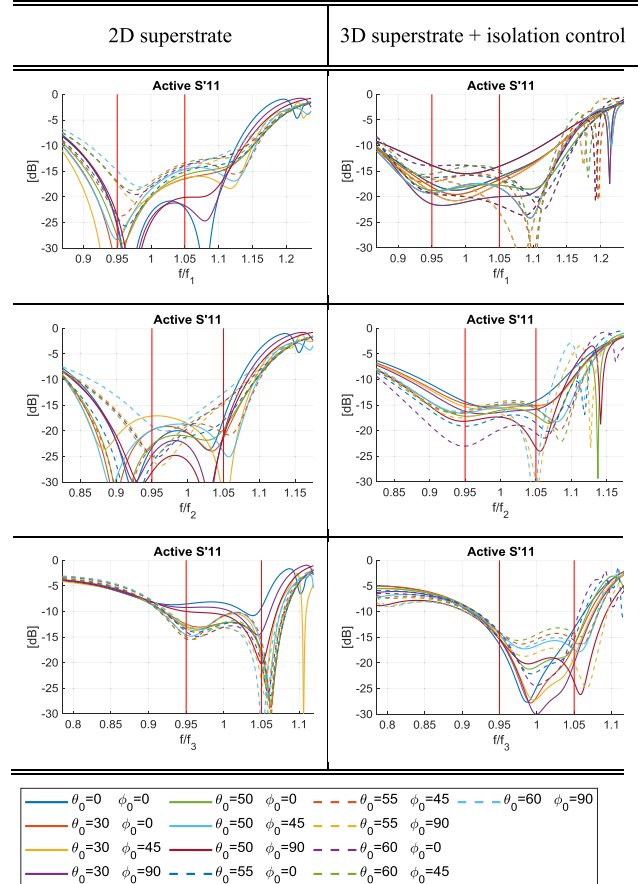


FIGURE 8. Active S'_{11} for the first three optimization cases from table 2 (2D superstrate & 3D superstrate).

The optimization resulted in very different performances for the different optimization scenarios. Considering the lower part of the band (center frequencies f_1 and f_2 with 10% bandwidth), the 2D superstrate and the 3D superstrate exhibit similar performances. Now considering the upper

part of the band (center frequencies f_3 with 10% bandwidth) and the higher bandwidth ratio (center frequencies f_2 with 20% bandwidth), the 3D superstrate clearly exhibits better behavior in controlling the active reflection coefficient and XPD. It clearly acts as a degree of freedom, as expected.

Starting from now, we give all the details of the optimization case considering the 10% bandwidth around the upper frequency f_3 for the cell with the 3D superstrate and isolation since it offers great improvement over the 2D superstrate. The optimization results are in table 3.

TABLE 3. Synthesized Reactive Loads & Generators Impedance GOALS: Minimizing active (S11, S22, S21, S12) and maximizing XPD.

Parameter Name	Value [Z]
Z_{g1} (Port 1 Generator impedance)	46.9-48.1i Ω
Z_{g2} (Port 2 Generator impedance)	46.9-48.1 Ω
Port 3 reactive load (side monopole)	0+102i Ω
Port 4 reactive load (side monopole)	0+102i Ω
Port 5 reactive load (corner monopole)	0-1380i Ω
Port 6 reactive load (dipole)	0+878i Ω
Port 7 reactive load (dipole)	0+878i Ω
Port 8 reactive load (isolation control)	0+853i Ω

The reactive loads connected to the parasitic elements generate reflection coefficients (equation 1) whose phases are:

- Port 3&4: 52°
- Port 5: -4°
- Port 6&7: 7°
- Port 8: 7°

An arraying of the considered unit cell with its 3D superstrate is shown in Fig. 9 to illustrate the superstrate architecture.

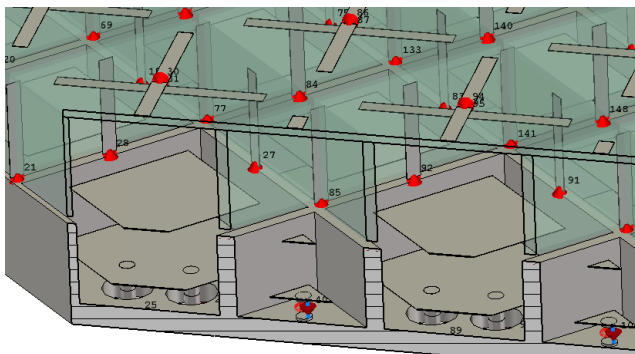


FIGURE 9. Array lattice of the dual-polarized IPAA unit cell.

This numerical design is meant to be a demonstration of the methodology in a complex optimization case with a simple numerical design. It is given with all data and dimensions necessary to whoever wants to reproduce it for verification purposes.

Figures 10a and 10b show the smith chart representations of the active impedance of the unit cell (Fig. 7b). This representation enables the reader to see the co-location of the active

impedances near the conjugate generator impedance when the other port is loaded with Z_g (Fig. 10a shows the active S11 when the port 2 is loaded with Z_{g2} & Fig. 10b shows the active S22 when the port 1 is loaded with Z_{g1}). It is clear that minimizing the dispersion of these active impedances is successful and those curves are collocated around the complex conjugate of a generator with impedance $Z_{g*} = 46.9 + 48i\Omega$.

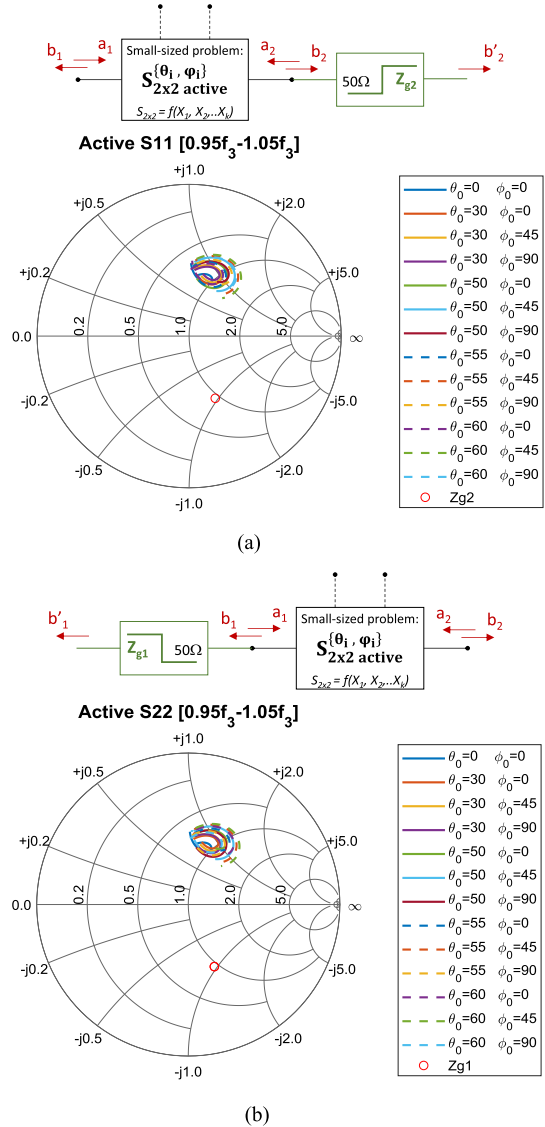


FIGURE 10. a) Smith chart representation of the proposed IPAA active S11 for different $\{\theta_i, \varphi_i\}$ over the bandwidth. Z_{g2} represented by a red dot. b) Smith chart representation of the proposed IPAA active S22 for different $\{\theta_i, \varphi_i\}$ over the bandwidth. Z_{g1} represented by a red dot.

Figure 11 represents the active scattering matrix when both active ports are normalized with the corresponding generator impedances Z_{g1} and Z_{g2} . It shows that the active $|S'_{11}|_{dB}$ and active $|S'_{22}|_{dB}$ of the unit cell are kept below $-13.2dB$ in the worst case and below $-20dB$ for a large set of scanning angles. Furthermore, the active coupling between the two feeding probes of the cell (active $|S'_{12}|_{dB}$ and active $|S'_{21}|_{dB}$) was kept below $-13.1dB$ (13.1dB isolation) in the worst

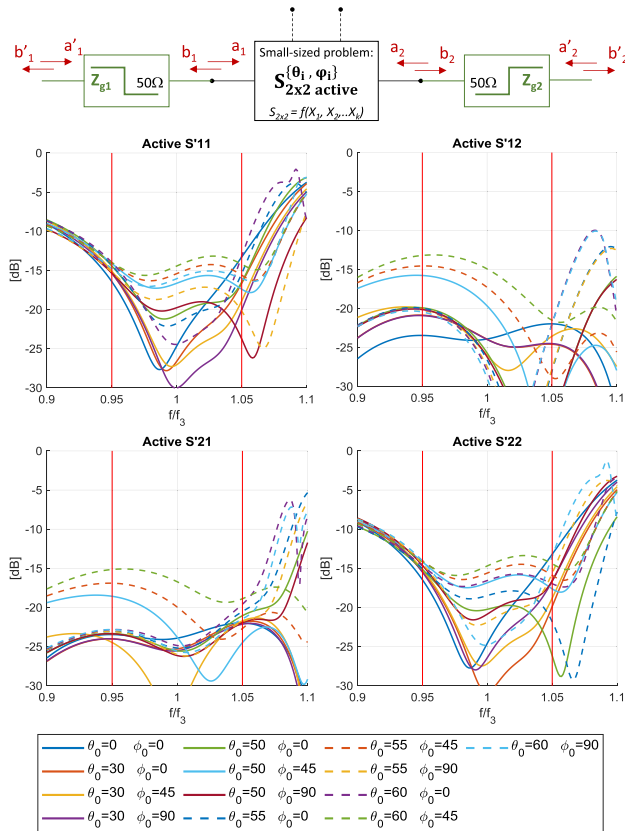


FIGURE 11. Proposed IPAA active scattering matrix.

case (D plane) and well below -20 dB when scanning the E- and H-planes.

Figures 12 shows the XPD for both feeding ports of the cell. It is maintained above 18.1dB in the worst case, which is close to the 20 dB objective that we set at the beginning of the optimization.

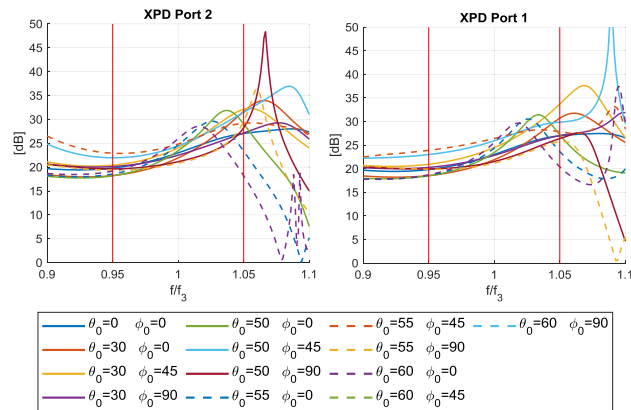


FIGURE 12. Proposed IPAA XPD for both active ports, considering different $\{\theta_i; \varphi_i\}$ over the bandwidth.

The different results shown in this part illustrate the interest and the versatility of the design methodology. The next step would be to find design solutions that emulate the optimal

generator impedances to connect the active ports of the unit cell. Such solutions are explored in III.

III. DESIGN OF A 5G UNIT CELL USING THE IPAA CONCEPT FOR A LARGE ANTENNA ARRAY

A. SPECIFICATIONS

In order to build a first proof of concept, a unit cell working in the new 5G band, especially in the C-band between 3.4GHz and 3.8GHz (11%) has been chosen. The unit cell will be associated to a 0.53λ step triangular lattice to avoid grating lobes in the scanning range. The driven element delivers a single linear polarization for simplicity and cost reduction.

The main challenge of this design is to obtain both a wide scanning range that we want to address and a simple technological process. Therefore, the 3D superstrate with vertical parasitic elements is removed to use a classical PCB stack. It is also a way to show if enough degrees of freedom are available, i. e enough parasitic elements, to reach the EM performances. The goal is to optimize the unit cell over a pointing range from $\theta_0 = 0^\circ$ to $\theta_0 = 70^\circ$ whatever the azimuth plane (i.e. $\varphi \in [0^\circ; 360^\circ]$). Such beamsteering specifications are especially interesting in dense urban 5G applications.

B. DESIGN PROCESS

At first, a low frequency dispersion driven array is chosen, based on a cavity backed stacked patch. It is fed through a compact U-shaped coupled aperture (Fig. 16a). We chose this architecture of elements because it shows a good impedance stability over the 5G C-band and because this architecture is quite low profile.

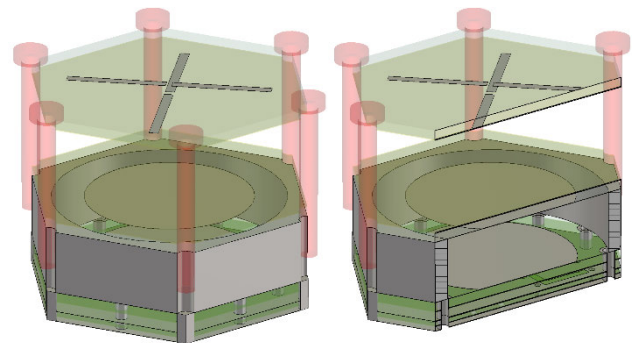


FIGURE 13. Unit cell of the proposed 5G IPAA before designing the matching network.

The low frequency dispersion optimization was checked over a small beam scan ($\pm 30^\circ$), to ensure the energy acceptance of the driven element and the effects of arraying in a normal operation. All elements are printed on a Taconic TLY-5 PCB with $\{\delta\epsilon_r = 2.2; \tan = 0.0009\}$ and a 1.524mm thickness, except for the two PCBs holding the feeding stripline which are 0.762mm.

A low complexity functionalized superstrate was considered to simplify prototyping and to reduce its cost.

The superstrate is thus composed of two orthogonal dipoles printed on both sides of a PCB lying 16 mm above the upper patch PCB. Both dipoles are centered in the middle of the unit cell to keep as much symmetries in the design as possible, as presented in Fig. 13.

The active scattering matrix of the cell was then calculated using Floquet’s formalism for about ten scan angles. The optimum reactive loads to connect to the parasitic elements were synthesized using the optimization method described in part. II.B. The optimization for the reactive loads results in a capacitor $C = 21.2\text{pF}$.

This capacitance effect was introduced in the design by optimizing the shape of the parasitic dipoles. We used the methodology used by Fouany *et al.* [18], which allows synthesizing a reactive load by changing the length of the dipole. Another solution would have been using SMD components [19]–[20] but shape optimization is cheaper and more reliable. The total dipoles length was changed from 25mm to 32.7mm to emulate the equivalent reactive load by shape optimization.

The performances of this unit cell in terms of active reflection coefficient and XPD are given in the fig. 14 and 15. Hence, the active impedance of the unit cell is stabilized near the complex impedance $Z_g^* = 14-13i\Omega$.

The XPD was not an optimization criterion in this design. The curves showing the lower XPD correspond to the diagonal plane ($\varphi = 45^\circ$). This is an expected behavior of patch arrays which exhibit a lower XPD on the diagonal planes. The other planes show great XPD above 20dB.

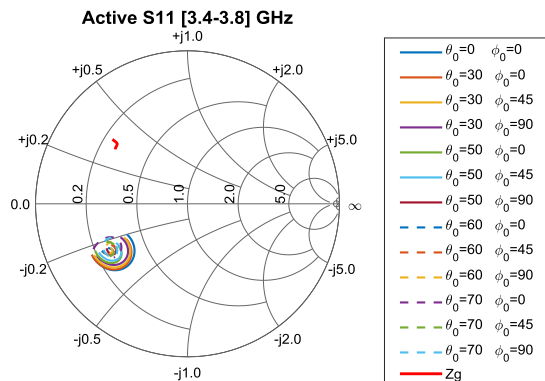


FIGURE 14. Active impedance of the proposed 5G IPAA before integrating the matching network—a small frequential dispersion is noticed.

Then a two-stub matching circuit is designed with the objective to present the generator impedance Z_g to the stripline access port of the cell.

The matching circuit is shown in Fig. 16b.

The final assembly of the unit cell considering all the mechanical elements and the feeding network is given in Fig. 18. The Rohacell spacer has been drilled to reduce its relative permittivity. Details of the Rohacell spacer are given in Fig. 23.

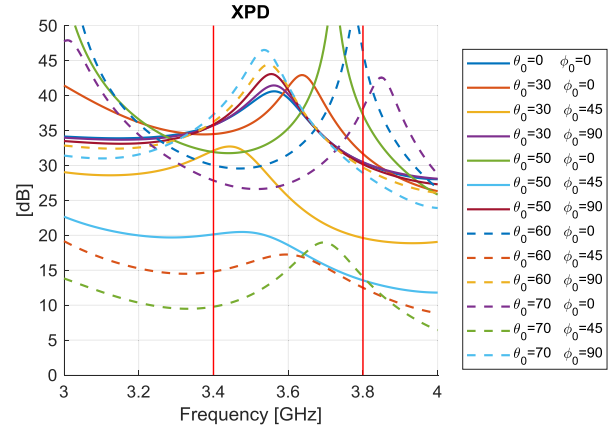


FIGURE 15. XPD of the proposed 5G IPAA before designing the matching network.

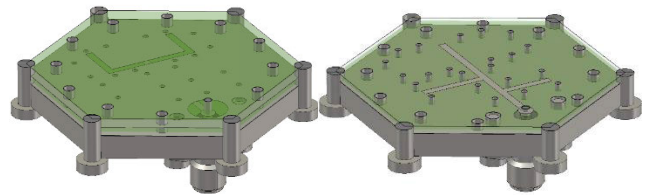


FIGURE 16. a) Feeding aperture of the proposed 5G IPAA. b) Feeding line and matching network of the proposed 5G IPAA.

The new simulations for the cell stacked with the matching circuit is plotted on Fig. 17a & 17b.

The simulated active reflection coefficient of the entire unit cell is kept below -13.6 dB (Fig. 17b) and the XPD is above 10 dB. The worst case is for the diagonal plane (Fig. 15). We remind that the XPD was not specified as a priority criterion for this optimization and there were few degrees of freedom to achieve the synthesis.

The dimensions of the unit cell are given in table 4 and the material characteristics used are given in table 5.

TABLE 4. Dimensions of the unit cell components.

Parameter Name	Value [mm]
Unit cell period	41.5
Rohacell height	15.74
Dipoles length	32.7
Upper patch radius	13.5
Lower patch radius	13.75
Metallic cavity height	10.25

TABLE 5. Different material characteristics.

Material name	Dielectric permittivity [ϵ_r]	Loss tangent [$\tan\delta$]
Rohacell	1.1	0.0016
Taconic TLY-5	2.2	0.0009

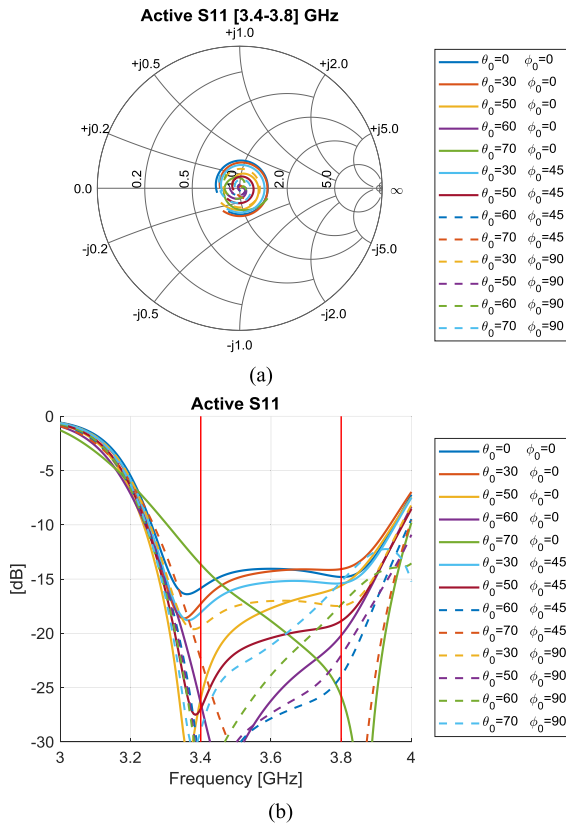


FIGURE 17. a) Smith chart representation of the active impedance of the proposed 5G IPAA. b) Cartesian representation of the active S11 of the proposed 5G IPAA.

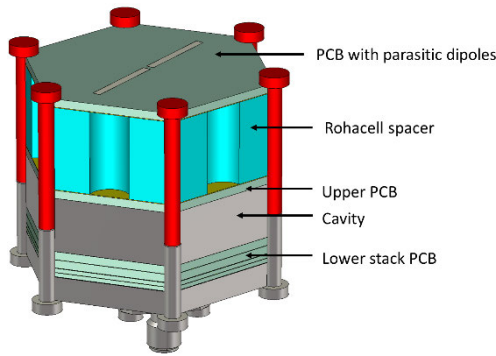


FIGURE 18. Unit cell of the proposed 5G IPAA.

Once the optimization is done, the unit cell active matching is evaluated for all possible scanning angles to evaluate the design performances [21].

The active reflection coefficient is computed by varying the periodic conditions phase shifts over 2π radians (Fig. 2). Larger phase shifts would present the non-radiative periodic solutions. The periodicity of these solutions are linked to the array period and they are drawn versus the wave vector in Fig. 19. Only the solutions inside the red circles can be radiated [17].

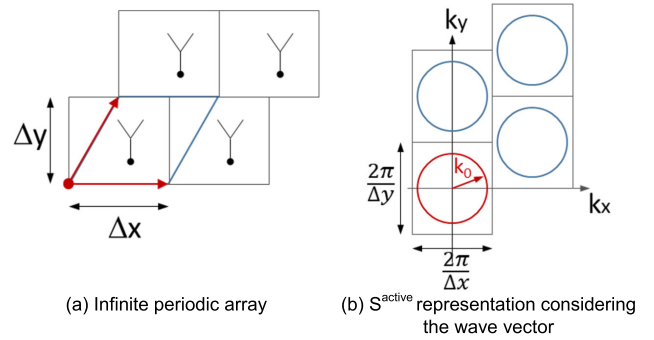


FIGURE 19. Calculation of the active reflection coefficient with the unit cell technique (a) gives periodic solutions in the wave vector domain (b).

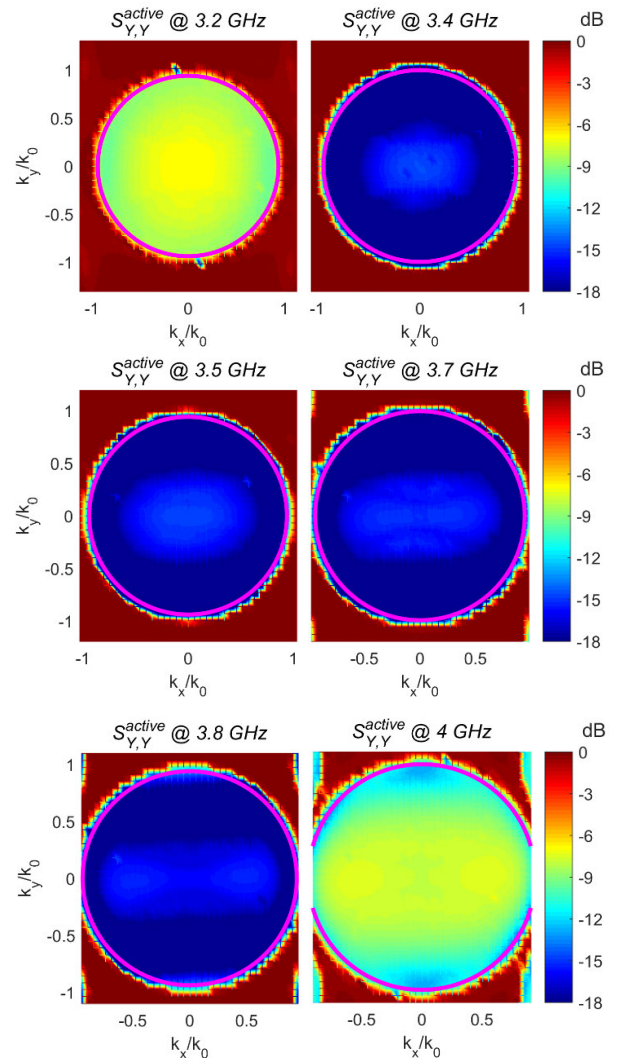


FIGURE 20. Circle diagrams showing active reflection coefficient as a function of k_x and k_y (transverse wave vector)—purple circle points $\theta_0 = 70^\circ$.

The active reflection coefficient is simulated with the unit cell method from 3.2 GHz to 4 GHz. It is plotted in Fig 20.

The circle diagrams show the active reflection coefficient for the phase conditions applied between the cells. Hence,

every concentric circle represents all the φ angles for a given θ_i . The center of each graph $\{k_x = 0; k_y = 0\}$ is broadside ($\theta_0 = 0^\circ$) and the purple circle marks $\theta_{max} = 70^\circ$.

It clearly appears that the active reflection coefficient is maintained really low (i.e., -13 dB) for the whole scanning range in the optimization bandwidth (3.4 to 3.8 GHz).

The efficiency of this unit cell has been evaluated in Fig.21 and it is between -0.1 and -0.3 dB for the worst case.

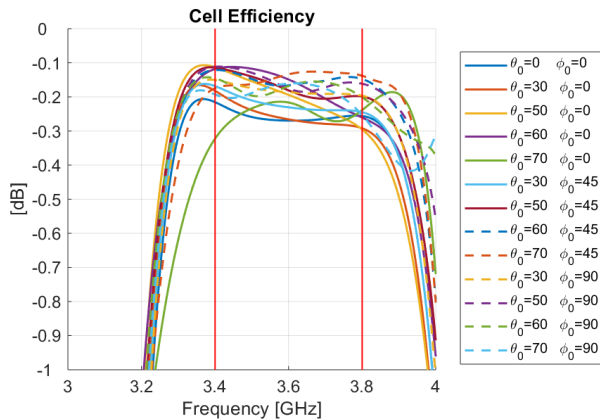


FIGURE 21. Total efficiency of the unit cell depending on its active matching for different directions on the frequency range.

Notice that this efficiency of the unit cell is defined by the power transmitted from the cell to the Floquet’s port, relatively to the incident power in the excitation port of the periodic cell.

The results confirm that the IPAA unit cell has been optimized and shows great performances compared to the given specifications. The manufactured prototype is presented in IV.

IV. PROTOTYPING AND MEASUREMENTS OF A SUB-ARRAY

To simplify the manufacturing process and for future applications, the prototype is defined by a 12-element tile, enabling the possibility to build a larger array (Fig. 22). Furthermore, this size of the structure is a good first step in validating the concept. Indeed, it is close to the maximum structure size we can simulate with a full-wave simulator installed on a workstation with a GPU. Therefore, a detailed comparison of the results obtained with the proposed method can be made with both a full-wave simulation and measurements.

The tile is the first step of the array construction. Because of its shape, many tiles can be assembled to build bigger and bigger arrays. The goal after this validation will be to manufacture more tiles to create larger arrays based on this tile architecture. An example of a larger array is shown in Fig. 23.

The unit cell was designed considering an equivalent effective permittivity $\epsilon_{eff} = 1.06$ for the Rohacell layer in order to be close from an ideal vacuum spacer. To this end, a Rohacell 71 HF foam ($\epsilon_r = 1.1$) has been modified by including

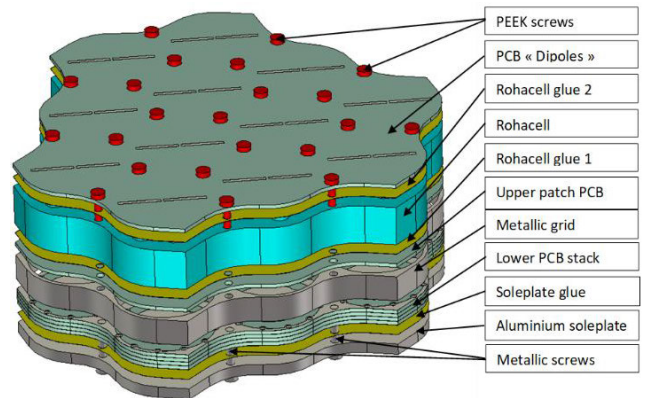


FIGURE 22. 12-element tile with its different components.

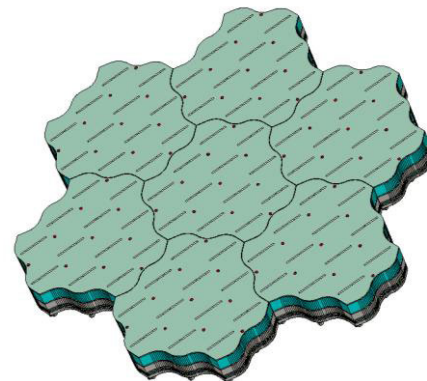


FIGURE 23. 84 elements array composed of 7 tiles.

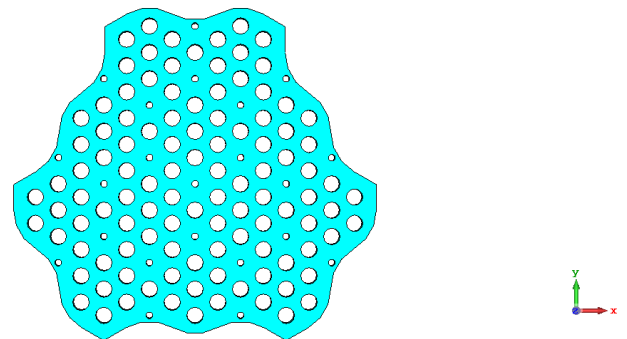


FIGURE 24. Rohacell layer with holes to reduce the equivalent ϵ_{eff} .

air holes. This technique has several advantages. At first, the equivalent effective permittivity of the material can be decreased while keeping a rigid foam and then the dielectric constant of the equivalent material is stabilized, meaning that the design will be more resilient to a dielectric constant dispersion inside the initial medium.

A picture of the fully mounted tile is given in Fig. 25. Three identical ones have been assembled to check the dispersion and to definitively validate the manufacturing process.

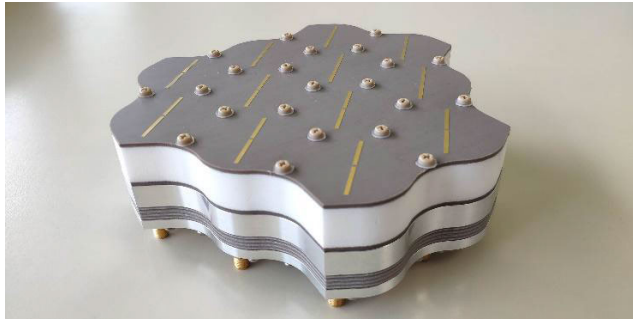


FIGURE 25. Photograph of a complete tile assembled.

The data used to plot the active reflection coefficient in Fig. 20 can be used to extract the coupling matrices from a large antenna array composed of up to several hundreds or thousands of cells. Using equation (12) [22], it is possible to build the complete scattering matrix of the array using the computed active reflection coefficient of the unit cell.

$$S_{m,n} = \frac{\Delta x \cdot \Delta y}{4 \cdot \pi^2} \cdot \int_{-\frac{\pi}{\Delta x}}^{\frac{\pi}{\Delta x}} \int_{-\frac{\pi}{\Delta y}}^{\frac{\pi}{\Delta y}} S_{Y,Y}^{active}(k_x, k_y) \cdot \exp^{-i[k_x \cdot (x_m - x_n) + k_y \cdot (y_m - y_n)]} \cdot \partial k_y \cdot \partial k_x \quad (12)$$

We name this formalism, the extraction of the S matrix from the periodic modeling.

Figure 27 shows the comparison between the measured and simulated reflection coefficient of an access port of the tile using a full-wave simulation and the reconstructed scattering matrix, based on port labeling in Fig. 26. Notice that the chosen port is not on the edge to be compliant with the chosen formalism. The measurements of the three tiles show a high agreement with the simulations, even for this small tile, which means that the manufacturing processes and the IPAA concept are validated.

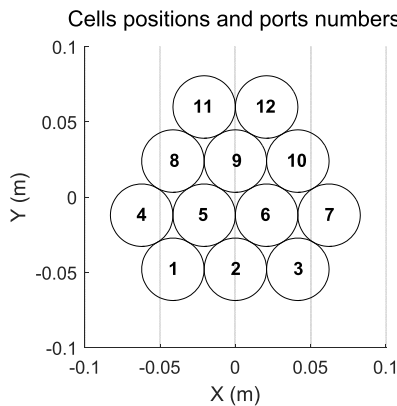


FIGURE 26. Position and numbering of cells in a tile.

The full-wave calculation also gives the directivity of a central element of the tile (port 9). Figure 28 maps the 2D AEP directivity over the optimized frequency bandwidth. The directivity of the center element is always kept above 1 dBi for any radiation direction in the optimized scanning range.

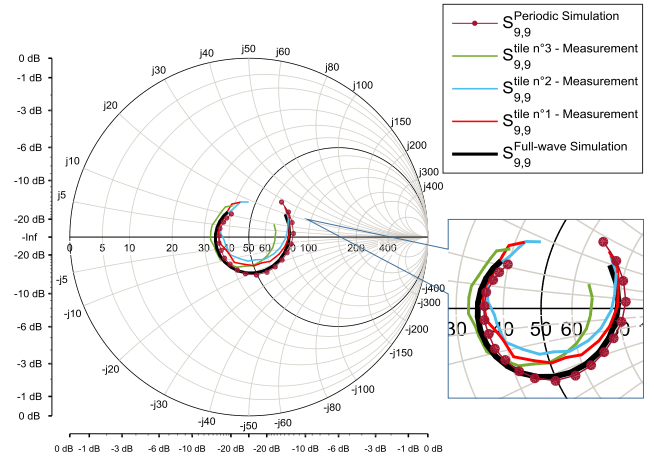


FIGURE 27. Smith chart representation of the reflection coefficient of port number 9: S parameter calculated 1/ from the periodic modeling, 2/ from measurements on each of the three assembled tiles, and 3/ from full-wave simulation.

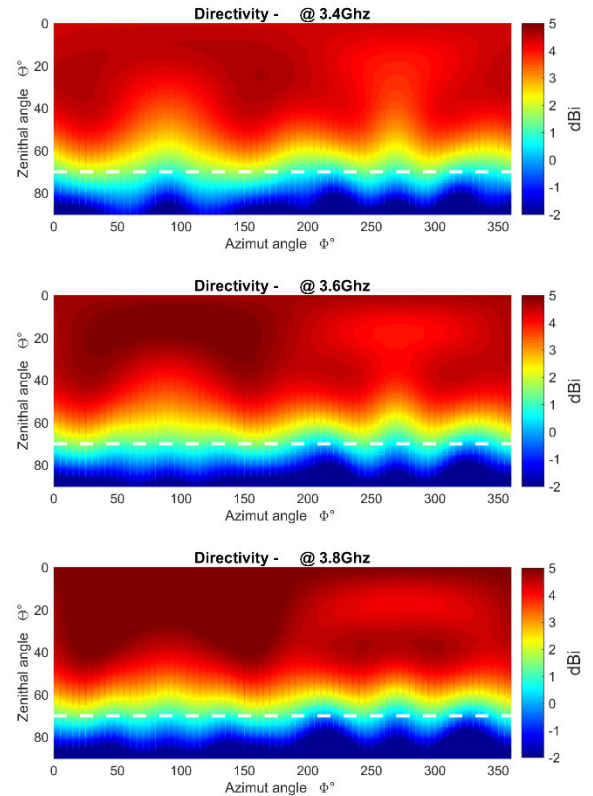


FIGURE 28. Simulated active element pattern of the element number 9 from the tile.

The directivity shows a great stability for each azimuthal angle and for every frequency in the optimization band. The main objective of this work was to define an efficient approach to optimize the active reflection coefficient of an antenna array for wide scan angles. Due to the link between this parameter and the active element pattern, a good optimization leads to a good stability of the pattern, whatever the azimuthal angle, as observed here.

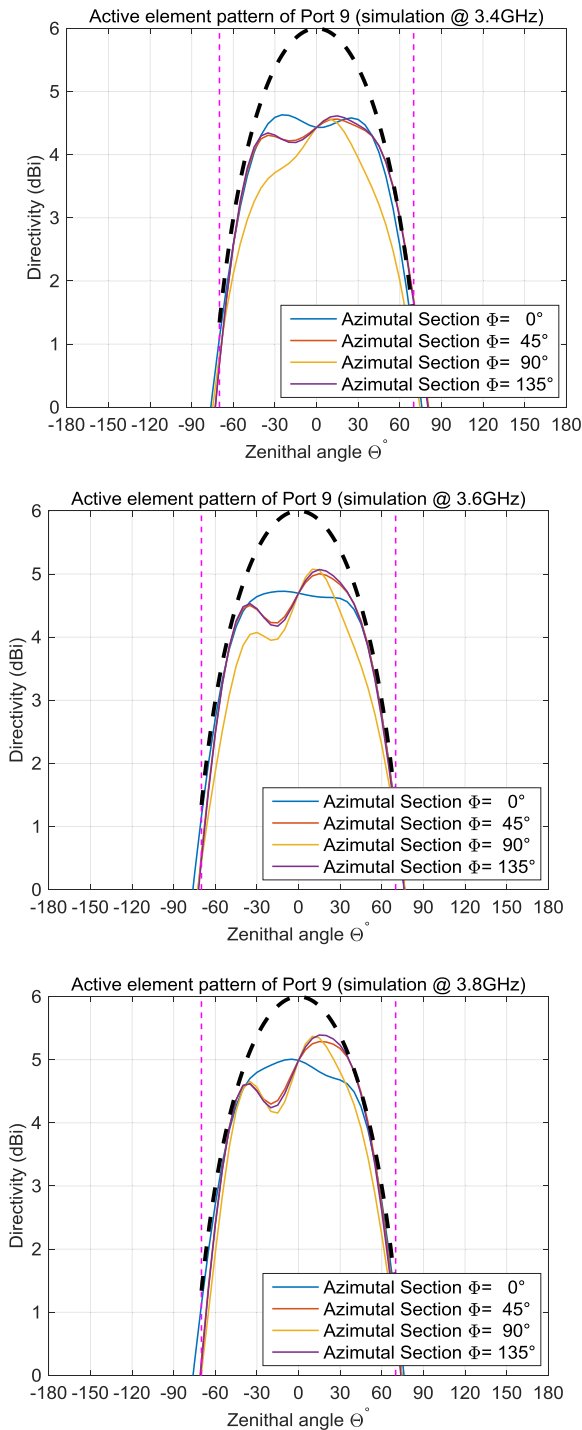


FIGURE 29. Simulated radiation pattern of the element number 9 from the tile represented with the $\cos\theta$ envelope (black dashed lines).

It was mentioned in part. II that the ideal AEP should tend toward a $\cos\theta'$ shape [15], [16]. Fig. 29 compares Cartesian representations of the directivity radiation patterns of port 9 with the directivity of a $\cos\theta'$ -shaped radiation pattern (black dashed line). The simulated diagrams seem to confirm that the ideal AEP is about to be realized. The ripple observed in simulations is due to the small size of the array considered here, since it is a single tile of twelve elements.

V. ARRAY-SIZE EFFECTS AND S PARAMETERS EXTRACTION

In order to validate bigger array arrangements, the three manufactured tiles were arranged to form the array presented

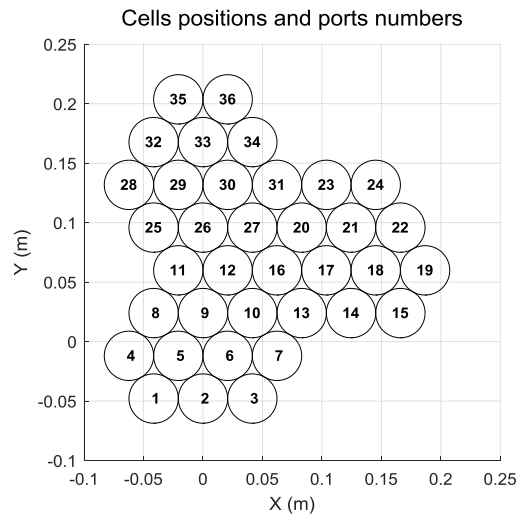
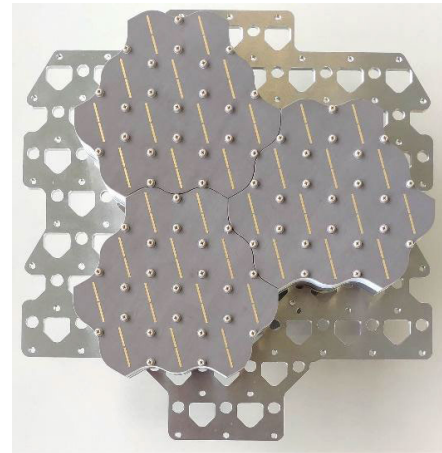


FIGURE 30. Position and numbering of the different elements of the 3-tile array.

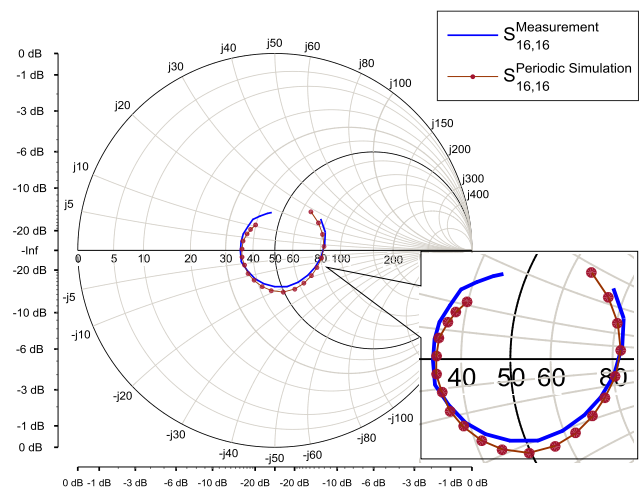


FIGURE 31. Smith chart representation of the reflection coefficient of port number 16: simulation versus 3-tile array measurement.

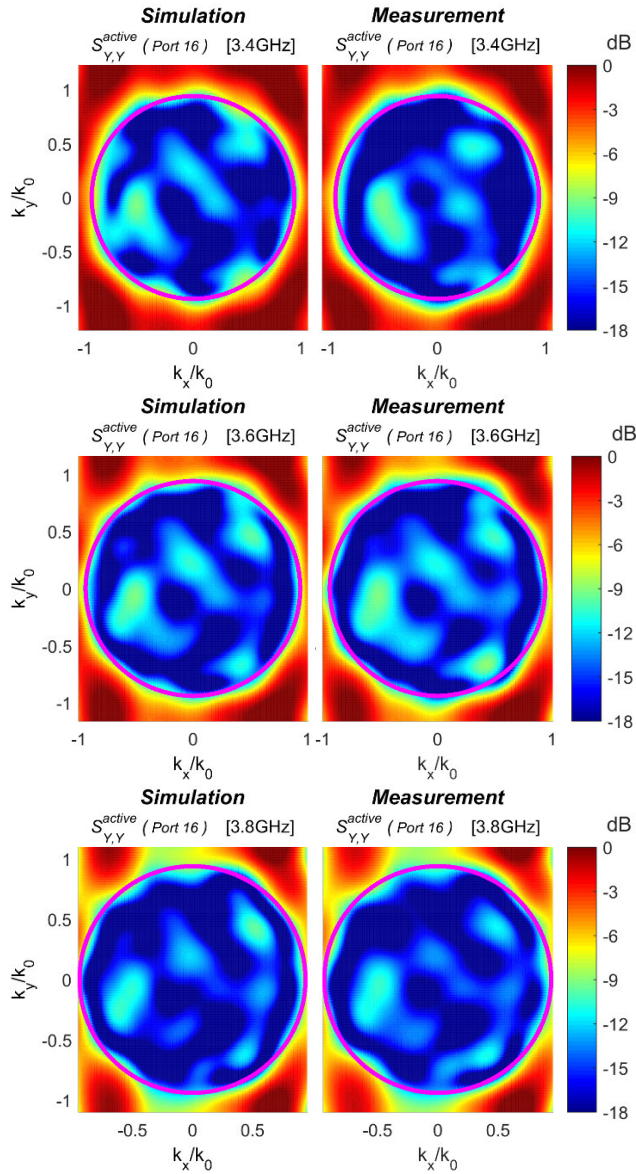


FIGURE 32. Active reflection coefficient of the central port (16) of the 3-tile array (left, simulation–right, measurement).

in Fig. 30. The full [S]-matrix of the 36 elements array was measured with a multiway VNA (working up to 49 channels [23]). The result for a central element ($|S_{16,16}|_{dB}$) is shown in Fig. 31, where it is compared to the $|S_{16,16}|_{dB}$, in red, deduced from the periodic modeling using (12). A good agreement is observed, as for the single tile.

The measured [S] matrix of this 36-cell finite-size array was used to assess the active reflection coefficients for all cells through (13) [22].

$$S_{Y,Y}^{active}(k_x, k_y)^{(port\ m)} = \sum_n S_{m,n} \cdot \exp^{-i[k_x \cdot (x_n - x_m) + k_y \cdot (y_n - y_m)]} \quad (13)$$

Figure 32 illustrates the dependence of the active reflection coefficients on the scan angle for the 3-tile prototype. This

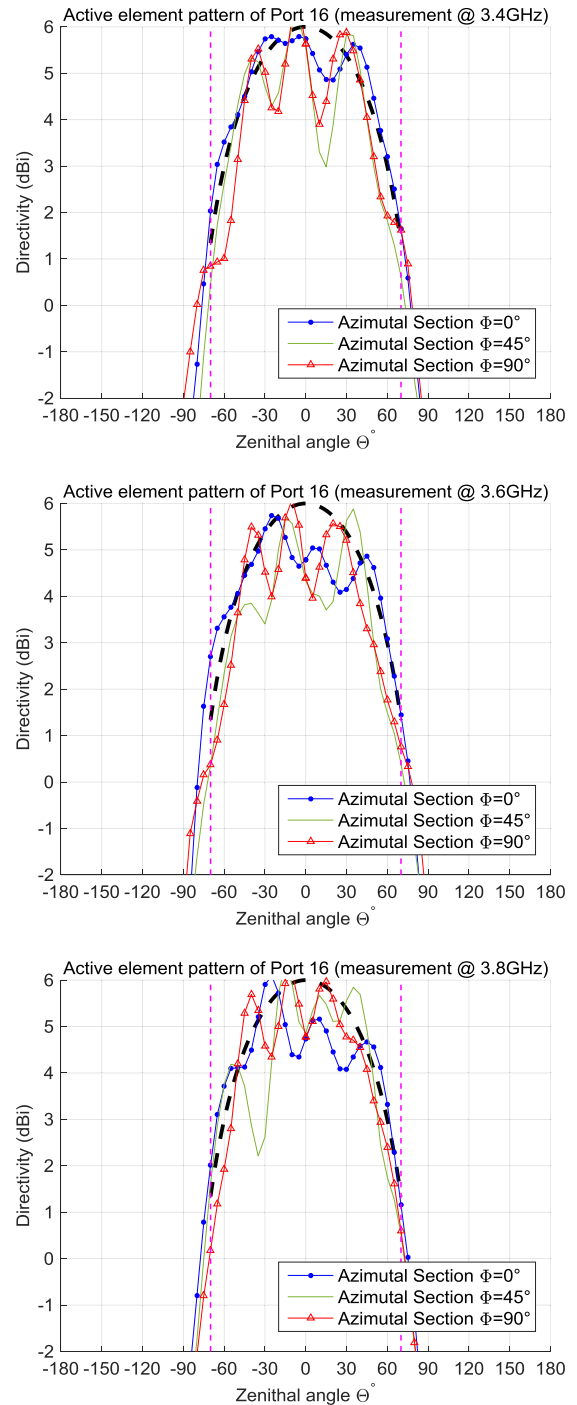


FIGURE 33. Measured AEP of the element nr 16 from the three-tile array.

illustration compares the simulated and measured S_{active} for port 16, which is approximately in the center of the array. The objective scanning range ($\theta_0 = 70^\circ$) is indicated by the purple circle.

The simulation and measurement show high agreement and good performances of the central cell even though the array is relatively small. Indeed, a larger array would exhibit performances closer to that of Fig. 20.

Figure 33 plots the directivity diagram for this central element (number 16) with the ideal ‘ $\cos\theta$ ’-shape envelope (black dashed curve). Some perturbations are visible on the pattern. They are caused by the small size of the array measured but it is clear that this measured directivity radiation pattern is close to the targeted ideal ‘ $\cos\theta$ ’ envelope. These results definitively validate the proposed modeling approach and the IPAA concept.

Notice that Fig. 33 shows more ripples than Fig. 29. This is because of the increased number of array elements. The ripple level appears to be higher than expected in some part of the angular spectrum, but it can be mainly explained by the oversized metallic fixture used for the three-tile configuration measurement (Fig. 30). It was not considered in simulations.

VI. CONCLUSION

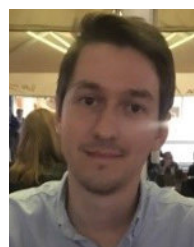
This paper described the benefit of the Interleaved Parasitic Arrays Antenna (IPAA) concept to minimize the active reflection coefficient over a wide scanning range. A methodology has been developed to implement the IPAA concept and this methodology is reliable and efficient in terms of computation time and obtained performances. This concept can be applied to many architectures of antenna arrays and to very different specifications to get the best for every specific applications.

The IPAA concept is based on two powerful ideas. The first singular property of the IPAA is to use parasitic elements as interleaved arrays, without increasing the step of the array lattice. The second singular property is to consider the generator impedance as a way to optimize the array performances. These elements act as degrees of freedom in the optimization to obtain both an active reflection coefficient as low as possible and a quasi-ideal ‘ $\cos\theta$ ’ active element pattern.

A numerical dual-polarization design was proposed to show the possibilities offered by this concept and a C-band prototype was built to validate the performances, showing great correspondence between simulations and measurements, thus validating the IPAA concept. A unit cell for a large antenna array with 11% bandwidth and scanning range up to $\theta_0 = 70^\circ$ has been presented, showing a very good active reflection coefficient below -13.6 dB and a satisfactory XPD in the whole operating range.

REFERENCES

- [1] Z. Iluz, R. Shavit, and R. Bauer, “Microstrip antenna phased array with electromagnetic bandgap substrate,” *IEEE Trans. Antennas Propag.*, vol. 52, no. 6, pp. 1446–1453, Jun. 2004.
- [2] E. Adas, F. De Flaviis, and N. G. Alexopoulos, “Realization of scan blindness free finite microstrip phased arrays based on mode-free radiating electromagnetic bandgap materials,” *IEEE Trans. Antennas Propag.*, vol. 66, no. 7, pp. 3375–3382, Jul. 2018.
- [3] S. Xiao, M.-C. Tang, Y.-Y. Bai, S. Gao, and B.-Z. Wang, “Mutual coupling suppression in microstrip array using defected ground structure,” *IET Microw., Antennas Propag.*, vol. 5, no. 12, pp. 1488–1494, 2010.
- [4] S. Stein, “On cross coupling in multiple-beam antennas,” *IRE Trans. Antennas Propag.*, vol. 10, no. 5, pp. 548–557, 1962.
- [5] P. Hannan, “The element-gain paradox for a phased-array antenna,” *IEEE Trans. Antennas Propag.*, vol. AP-12, no. 4, pp. 423–433, Jul. 1964.
- [6] W. Kahn, “Ideal efficiency of a radiating element in an infinite array,” *IEEE Trans. Antennas Propag.*, vol. AP-15, no. 4, pp. 534–538, Jul. 1967.
- [7] G. Oliveri, M. Salucci, N. Anselmi, and A. Massa, “Multiscale system-by-design synthesis of printed WAIMs for waveguide array enhancement,” *IEEE J. Multiscale Multiphys. Comput. Tech.*, vol. 2, pp. 84–96, 2017.
- [8] J. T. Logan, R. W. Kindt, M. Y. Lee, and M. N. Vouvakis, “A new class of planar ultrawideband modular antenna arrays with improved bandwidth,” *IEEE Trans. Antennas Propag.*, vol. 66, no. 2, pp. 692–701, Feb. 2018.
- [9] D. Cavallo, W. H. Syed, and A. Neto, “Connected-slot array with artificial dielectrics: A 6 to 15 GHz dual-pol wide-scan prototype,” *IEEE Trans. Antennas Propag.*, vol. 66, no. 6, pp. 3201–3206, Jun. 2018.
- [10] A. A. Manga, R. Gillard, R. Loison, I. L. Roy-Naneix, and C. Renard, “Implementation of a correcting coupling mechanism to mitigate surface wave in phased arrays,” in *Proc. 12th Eur. Conf. Antennas Propag. (EuCAP)*, London, U.K., 2018, pp. 1–4.
- [11] B. Sadhu, X. Gu, and A. Valdes-Garcia, “The more (antennas), the merrier: A survey of silicon-based mm-wave phased arrays using multi-IC scaling,” *IEEE Microw. Mag.*, vol. 20, no. 12, pp. 32–50, Dec. 2019.
- [12] A. H. Aljuhani, T. Kanar, S. Zahir, and G. M. Rebeiz, “A scalable dual-polarized 256-element Ku-band phased-array SATCOM receiver with $\pm 70^\circ$ beam scanning,” in *IEEE MTT-S Int. Microw. Symp. Dig.*, Jun. 2018, pp. 1203–1206.
- [13] D. M. Pozar, “The active element pattern,” *IEEE Trans. Antennas Propag.*, vol. 42, no. 8, pp. 1176–1178, Sep. 1994.
- [14] R. Harrington, “Reactively controlled directive arrays,” *IEEE Trans. Antennas Propag.*, vol. AP-26, no. 3, pp. 390–395, May 1978.
- [15] S. P. Skobelev, *Phased Array Antennas With Optimized Element Patterns*. Norwood, MA, USA: Artech House, 2011.
- [16] S. P. Skobelev, “On the ideal gain of a radiating element in a planar array,” in *Proc. 12th Int. Conf. Math. Methods Electromagn. Theory*, Jun. 2008, pp. 305–307.
- [17] A. K. Bhattacharyya, *Phased Array Antennas: Floquet Analysis, Synthesis, BFNs and Active Array Systems*. Hoboken, NJ, USA: Wiley, 2006.
- [18] J. Fouany, M. Thevenot, E. Arnaud, F. Torres, C. Menudier, T. Monediere, and K. Elis, “New concept of telemetry X-band circularly polarized antenna payload for CubeSat,” *IEEE Antennas Wireless Propag. Lett.*, vol. 16, pp. 2987–2991, 2017.
- [19] F. Fezai, C. Menudier, M. Thevenot, C. Vollaive, N. Chevalier, and T. Monediere, “Reducing electronic device standby power using a remote wake-up system [antenna applications corner],” *IEEE Antennas Propag. Mag.*, vol. 58, no. 5, pp. 66–73, Oct. 2016.
- [20] M. Thevenot, C. Menudier, A. E. S. Ahmad, G. Z. E. Nashef, F. Fezai, Y. Abdallah, E. Arnaud, F. Torres, and T. Monediere, “Synthesis of antenna arrays and parasitic antenna arrays with mutual couplings,” *Int. J. Antennas Propag.*, vol. 2012, pp. 1–22, Apr. 2012.
- [21] A. Maati, C. Menudier, M. Thevenot, F. Torres, and T. Monediere, “Accurate scattering matrix reconstruction for multi element antennas—Application to hybrid arrays,” in *Proc. 12th Eur. Conf. Antennas Propag. (EuCAP)*, London, U.K., 2018, p. 5.
- [22] B. Lesur, A. Maati, M. Thevenot, C. Menudier, E. Arnaud, T. Monediere, C. Melle, D. Chaibault, and A. Karas, “A large antenna array for Ka-band satcom-on-the-move applications—Accurate modeling and experimental characterization,” *IEEE Trans. Antennas Propag.*, vol. 66, no. 9, pp. 4586–4595, Sep. 2018.
- [23] C. Menudier, E. Arnaud, M. Thevenot, F. Fezai, A. Oueslati, N. Chevalier, S. Reynaud, and T. Monediere, “Synthesis of multi-element antennas using a measurement test bench,” in *Proc. 45th Eur. Microw. Conf. (EuMC)*, Paris, France, Sep. 2015, pp. 6–11.



RÉMY LAMEY was born in Seclin, France, in 1994. He received the degree in electronics and telecommunications from IMT Lille Douai, Villeneuve d’Ascq, France, in 2018. He is currently pursuing the Ph.D. degree in high-frequency electronics with the Xlim Research Institute, in collaboration with Thales LAS, Limours, France. His main research interests include array antennas modeling and design, wide-angle scanning antennas, and RADAR.



MARC THEVENOT was born in Limoges, France, in February 1971. He received the M.Sc. degree in microwaves and Ph.D. degree in electronic from the University of Limoges, France, in 1995 and 1999, respectively.

He joined CNRS, in 2001. He is currently a Researcher with the XLIM Research Laboratory, RF Systems Group, University of Limoges. His main current research interests include the antenna arrays, reconfigurable active antennas, parasitic

element antennas, and reflectarrays.



CYRILLE MENUDIER (Member, IEEE) received the degree in electronics from ENSIL, in 2004, the M.S. degree in high-frequency telecommunications from the University of Limoges, the Ph.D. degree in telecommunications from the XLIM Research Laboratory, University of Limoges, in 2007, and the accreditation to supervise research (HDR) degree, in 2018. He was a Postdoctoral Fellow at CNES (French Space Agency), Toulouse, until 2009, where he worked

on reconfigurable reflectarray antennas. He is currently an Associate Professor of the RF systems axis with the XLIM Research Laboratory. His research interests include reconfigurable antennas, active antennas and phased arrays, reflectarrays, parasitic element antennas, and mutual coupling effects.



ERIC ARNAUD was born in France, in 1970. He received the Diplôme D'Etudes Supérieures Spécialisées (DESS) and Ph.D. degrees in electronics and telecommunication, with a focus on circularly polarized EBG antenna, from the University of Limoges, in 1994 and 2010, respectively. From 1996 to 2001, he has been in charge of the microwave part of free-electron laser (L.U.R.E). Since 2001, he has been in charge of the XLIM Laboratory's antenna test range. He participated

in several research projects related to the design, development, and characterization of antennas. His research interests include in the fields of circularly polarized antenna and isoflux pattern antenna.



OLIVIER MAAS was born in Metz, France, in 1960. He received the degree in electronics from ENSIEG, Grenoble, in 1982. He joined the Microwave Development Department, Thales, in 1983. Since 1995, he has been designing radiating elements and passive microwave circuits for AESA applications.



FAYCEL FEZAI (Member, IEEE) received the M.S. degree in high-frequency electronics and optoelectronics from France, in 2010, and the Ph.D. degree in telecommunications from the XLIM Research Laboratory, University of Limoges, in 2013. He is a Hardware Radio-Frequency Engineer with Thales Air Systems, France. His research interests include parasitic element antennas, spherical wave expansion development, reconfigurable antennas, antenna array, synthesis methods, retrodirective

antennas, dielectric resonator and power conversion circuits, and radio frequency/data communication.

...